

Calibration of bonded-particle model parameters and simulation of compression behavior for oilseed rape shoot stalks

Yiyin Shan¹, Qingxi Liao^{1,2*}, Xingyu Wan^{1,2}, Jiacheng Yuan¹, Yitao Liao^{1,2}, Daxin Gao^{1,2}

(1. College of Engineering, Huazhong Agricultural University, Wuhan 430070, China;

2. Key Laboratory of Agricultural Equipment in Mid-lower Yangtze River, Ministry of Agriculture and Rural Affairs, Wuhan 430070, China)

Abstract: The relationship between the parameters of the bonded-particle model and the macroscopic properties of oilseed rape shoot stalk provides valuable insights into the interaction between the stalks and harvesting machinery. In this study, a discrete element model of oilseed rape shoot stalk was constructed using a method that combined ordered and bimodal distribution filling. The model's six contact and five bonding parameters were calibrated based on physical and simulated diametral compression tests. The Plackett-Burman design was employed to screen the effects of the parameters on the rupture force. The range of significant parameters was determined using the steepest ascent test. Furthermore, by calculating the second-order regression model and analyzing the significance of parameter combination using the central composite design method, the optimal parameter combination was identified, including a bonded disk radius of 0.78 mm, a normal stiffness per unit area of 4.61×10^7 Pa, a shear stiffness per unit area of 5.21×10^7 Pa, and a coefficient of static friction between particles of oilseed rape shoot stalk of 0.47. The simulated rupture force (58.80 N) differed by 6.5% from the average value of the physical test (62.92 N), and the deformation of the compression process was consistent. The results demonstrate that the model effectively reflects the mechanical failure properties of oilseed rape shoot stalk during the diametral compression, providing a reference for modeling other crop stalks and aiding in the study of interactions between clamping-transporting devices and stalks during harvesting.

Keywords: oilseed rape shoot, discrete element model, ordered and bimodal distribution filling method, mechanical properties, parameter calibration

DOI: [10.25165/j.ijabe.20241706.8833](https://doi.org/10.25165/j.ijabe.20241706.8833)

Citation: Shan Y Y, Liao Q X, Wan X Y, Yuan J C, Liao Y T, Gao D X. Calibration of bonded-particle model parameters and simulation of compression behavior for oilseed rape shoot stalks. *Int J Agric & Biol Eng*, 2024; 17(6): 46–58.

1 Introduction

Oil-vegetable dual-use technology is a crucial production model for advancing China's oilseed rape industry. The Yangtze River Basin, which primarily cultivates double-low (low erucic acid and low glucosinolate) oilseed rape, accounts for over 85% of national production^[1,2]. During the bolting period, the main stem and its side branches are harvested as fresh vegetables or processed into dehydrated vegetables, rich in vitamin B1, vitamin C, zinc, and selenium. Additionally, harvesting oilseed rape shoots promotes the growth of practical branches, thus increasing the yield of rapeseed^[3].

Due to the high moisture content and crisp texture of oilseed rape shoot stalks (ORSS), it is essential to study their biomechanical properties and analyze the interaction between the clamping-transporting device of the oilseed rape shoot harvester (Figure 1) and the shoots during the harvest process. This analysis aimed to

minimize mechanical damage and enhance harvest quality, thereby providing technical support for the design of the clamping-transporting device.

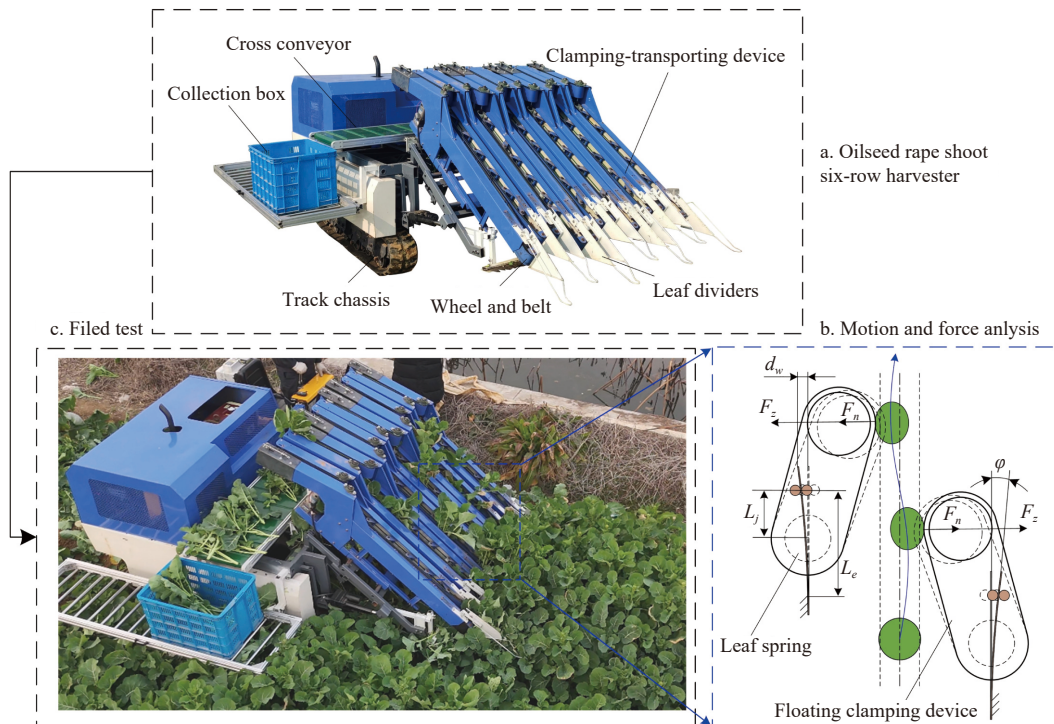
Furthermore, the bonded-particle model (BPM) is an effective method for describing particle breakage within the DEM simulation environment^[4,5], which has been utilized to investigate the breakage behavior of the flexible stem and crop stalk^[6-9]. For example, Zhao et al.^[10] and Wang et al.^[11] constructed the cylindrical models of cotton stalk and citrus fruit stalks, respectively, to effectively characterize bending and shearing forces using the Application Programming Interface (API) in EDEM software. In addition, Guo et al.^[12] generated a discrete element model of the compressed banana bunch stalk sample using the PFC^{3D} software, effectively visualizing the micromechanics and nonlinear damage behavior of the banana bunch stalk. To reflect the macroscopic interaction between corn cob biological tissues and the external environment, Li et al.^[13] proposed a modeling method and established a discrete element model for the upper, middle, and lower segments of the corn cob, treating them as a frustum with a narrow upper part and a wide lower part. These studies have validated the bonded particle model and provided insights into the damage behavior, failure characteristics, and micromechanical properties of materials.

The discrete element method regards bulk material as a collection of independent, interacting, and contacting particle units with assigned material properties^[14]. Defining micro-parameters, including intrinsic parameters, contact parameters between particles, contact parameters between particles and geometry, and bonding model parameters, is crucial for capturing the movement and deformation of the material and obtaining reliable simulation

Received date: 2024-01-29 **Accepted date:** 2024-11-01

Biographies: Yiyin Shan, PhD, research interest: harvesting technology and equipment of oilseed rape, Email: shanyiyin@foxmail.com; Xingyu Wan, Associate professor, research interest: harvesting technology and equipment of oilseed rape, Email: wanyxy@mail.hzau.edu.cn; Jiacheng Yuan, PhD, research interest: harvesting technology and equipment of oilseed rape, Email: yuanjiacheng.hzau@foxmail.com; Yitao Liao, Professor, research interest: technology and equipment of mechanized production of oilseed rape, Email: liaoetao@mail.hzau.edu.cn; Daxin Gao, PhD, research interest: technology and equipment of mechanized production of oilseed rape, Email: gaodx@mail.hzau.edu.cn.

*Corresponding author: Qingxi Liao, Professor, research interest: technology and equipment of mechanized production of oilseed rape. No.1 Shizishan Street, Hongshan District, Wuhan 430070, China. Email: liaoqx@mail.hzau.edu.cn.



Note: F_z was the force applied by the oilseed rape shoots on the floating clamping device; F_n was the clamping force; d_w was the deflection of leaf spring; ϕ was the rotation angle of the leaf spring; L_j was the moment arm; L_e was the effective length of leaf spring.

Figure 1 Schematic diagram of oilseed rape shoot six-row harvester

results^[4]. Micro-parameters are typically obtained through direct measurement, but their accuracy can be influenced by test conditions. Bonding model parameters are calibrated based on relevant theory and test standards. However, they require validation by comparing simulations with physical tests to ensure accurate simulation conditions^[15]. To enhance the calibration efficiency and accuracy of irregular particles, a test-simulation combined calibration method is proposed for defining the parameters of the BPM mode^[16,17]. For example, Shi et al.^[18] performed quasi-static tests to measure the compressive strength, elastic modulus, and shear strength, using these as response indices to calibrate bonding model parameters with the response surface method. The straw model accurately reflected the mechanical and failure properties of wheat straw. Due to differences in size, dimensions, and shapes of crops, the discrete element model constructed by combined calibration method of test-simulation effectively characterized their biomechanical properties. This method is widely applied to build discrete element models for crop flexible stalks and seeds^[19,18,5].

In this study, a discrete element model of oilseed rape shoot stalks with failure characteristics was established for the harvesting period. Additionally, a particle filling method combining ordered and bimodal distribution filling was proposed. The model's micro-parameters were calibrated using a diametral compression simulation test, and the simulation results were verified to reflect the compression behaviors of oilseed rape shoot stalks. This study provides a reference for simulating the interaction between harvesting machinery and oilseed rape shoot stalks.

2 Materials and methods

2.1 Structure of the oilseed rape shoot six-row harvester

As illustrated in Figure 1a, an oilseed rape shoot six-row harvester was developed using a gantry-type track chassis, driven by a hydraulic drive. Leaf dividers were positioned at the front of the belt-clamping conveyor device, where belts were mounted on

parallel clamping wheels. The clamping force was adjustable via a set of leaf springs. A reciprocating cutter was installed at the front of the frame, while a cross conveyor was located at the rear of the clamping-transporting device. During the harvesting operation, the leaf dividers effectively separated the oilseed rape shoots into rows. The cut shoots were then grasped by the clamping belts and transported upward along the frame. Finally, the shoots were transferred by the clamping belts to the cross conveyor and delivered to the collection box.

As shown in Figures 1b and 1c, during the clamping and transporting process, the floating clamping device exerted diametral compression on the oilseed rape shoot stalks, which is the primary cause of the mechanical damage. However, the micro-stress process was challenging to observe and analyze directly, necessitating an adequate simulation model to reflect the biomechanical properties and provide theoretical support for the design of clamping-transporting devices.

2.2 Materials preparation

This study investigated the physical and mechanical properties of ORSS using physical experiments and the discrete element method. The oilseed rape cultivar used was Huayouza 62 (*Brassica napus* L.). Samples were collected at a height of 150-350 mm from the ground and grown for 137 d (buds flush with the leaf blade apex) in the experimental field of Huazhong Agricultural University (30°28' N, 114°21' E) in China. The leaves were detached in the laboratory, and samples were divided into two groups. A TMS-Pro texture analyzer (Food Technology Corporation, USA) was used to perform three-point bending and diametral compression test, as shown in Figure 2. The average diameter of ORSS was estimated by measuring each stalk three times at the harvesting point near the middle of the test sample. Samples were tested in their original size and shape under fresh conditions within 24 h. The water content of specimens, ranging from 89.5 to 92.3%, was determined using a standard method before testing^[20].

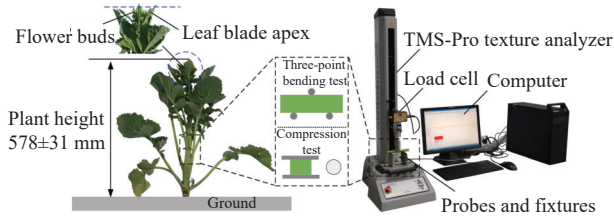


Figure 2 The sample location of oilseed rape stalk and test device

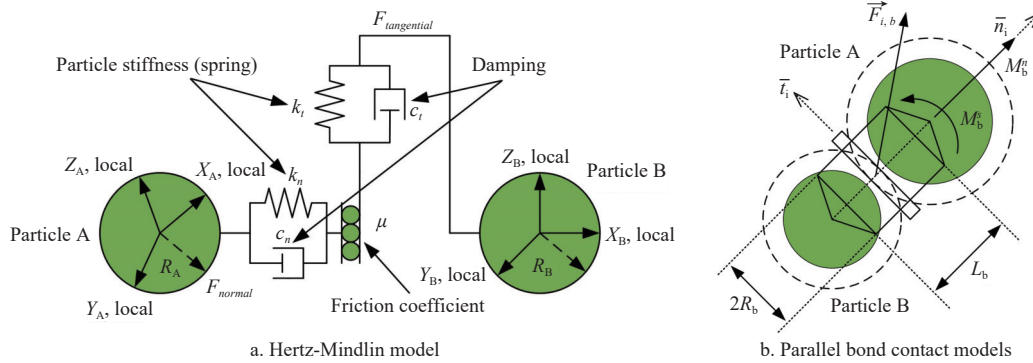
2.3 Preliminary discrete element model of ORSS

DEM captures the dual nature of granular media, which behaves like both a solid and a fluid, with bulk behavior emerging from the collective interaction of each particle. Based on previous research^[21,9,7], the Hertz-Mindlin model with bonding contact was employed to build the flexible ORSS to model the micromechanics of granular material. This model consists of two separate models: the Hertz-Mindlin model (Figure 3a) and the parallel bond contact model (Figure 3b). The particle system is composed of a finite number of discrete soft spheres that contact and detach from one

another, establishing a relationship regarding mutual movement, contact force, and energy. When the particles are bonded, the force $\delta \vec{F}_{i,b}$ and moments δM_i^b are adjusted incrementally every time step according to Equation (1).

$$\begin{aligned} \delta \vec{F}_{n,b} &= -k_b^n v_n A \delta_t \\ \delta \vec{F}_{t,b} &= -k_b^t v_t A \delta_t \\ \delta M_b^n &= -k_b^n \omega_n J \delta_t \\ \delta M_b^s &= -k_b^s \omega_t J \delta_t / 2 \end{aligned} \tag{1}$$

where, $\delta \vec{F}_{n,b}$ and $\delta \vec{F}_{t,b}$ are the normal force component and tangential force component of parallel bond, respectively; δM_b^n and δM_b^s are the normal moment component and tangential moment component of a parallel bond, respectively; k_b^n and k_b^t are stiffnesses in the normal and tangential directions, respectively; v_n and v_t are the relative velocities in the normal and tangential directions, respectively; R_b is the radius of the bond; δ_t is the time increments; $A = \pi R_b^2$ is the area of the contact area; $J = \pi R_b^4 / 2$ is the moment of inertia of the bond cross-section.



Note: $\vec{F}_{i,b}$ is the resultant force of particle A on particle B; L_b is the overlap of particle A and particle B; δM_b^n and δM_b^s are the normal moment component and tangential moment component of a parallel bond, respectively; R_b is the radius of the bond.

Figure 3 Schematic diagram of BPM model

The parallel bond was used to bond particles with a finite-sized glue bond, which resists normal and tangential movement up to predefined normal and tangential stress levels, at which point the bond breaks. Hence, the normal and tangential stress were computed and evaluated according to Equation (2).

$$\begin{aligned} \sigma_{\max} &= \frac{\vec{F}_{n,\text{total}}}{A} + \frac{2M_b^n}{J} R_b > \sigma_{cr} \\ \tau_{\max} &= \frac{\vec{F}_{t,\text{total}}}{A} + \frac{2M_b^s}{J} R_b > \tau_{cr} \end{aligned} \tag{2}$$

where, σ_{\max} and τ_{\max} are the maximum normal stress and maximum tangential stress, respectively; σ_{cr} and τ_{cr} are the tension strength and shear strength, respectively.

2.4 Construction of discrete element model of ORSS

During the harvesting period, the ORSS was crisp and tender and mainly consisted of cortex and pith, which were not lignified and hardened, respectively, as illustrated in Figure 4a. Therefore, the ORSS could be treated as a homogeneous and isotropic elastic body, and particles with the same microscopic parameters were used to model it^[11,15]. Figure 4b shows the cross-section of the ORSS as an approximate ellipse with average major ($2a$ -cross-section-width) and minor ($2b$ -cross-section-width) axes dimensions of (16.12 ± 0.75) mm and (15.64 ± 0.92) mm, respectively. To improve the computational efficiency of the Hertz-Mindlin model, the cross-section was simplified to a circle during the modeling process. Additionally, the cortex thickness was (1.80 ± 0.72) mm. Therefore,

the diameter and cortex thickness were taken as 15.0 mm and 1.8 mm, respectively, for the discrete element model of ORSS.

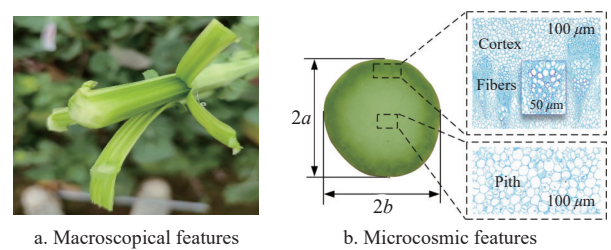


Figure 4 Structure of oilseed rape shoot

Based on the modeling methods of relevant scholars, the particle size distribution of spherical particles for random filling methods include mono, Gaussian, and bimodal distributions^[22]. These varying distributions result in different particle numbers, filling rates, and different lengths and quantities of bonding bonds between particles^[23], as shown in Figure 5. The mono distribution consists of spherical particles of equal size with bonds distributed around them; this configuration cannot accurately describe the mechanical properties^[15]. The distribution and the number of spherical particles of the Gaussian distribution are determined by the particle size and the standard deviation. This distribution features particles of varying sizes with sparsely distributed bonding bonds that better reflect the mechanical properties compared to the mono distribution. Additionally, the bimodal distribution,

characterized by two distinct peaks, offers advantages for accurately modeling particle size distribution^[24]. It provides the best potential for achieving high packing density and favorable breakage characteristics with a minimal number of spherical particles^[15], ensuring good bonding strength in the model.

To improve the accuracy of the discrete element model of ORSS, the complex solid geometrical structure of the ORSS was constructed by combining ordered and bimodal distribution filling methods. The ordered filling method with uniform particle size was used for the cortex part, while the pith part was constructed using the bimodal distribution method. Additionally, the non-structured particle distribution for the pith part effectively reduces the effects

of the breaking planes of the cortex on the cross-section breakage and the dependency on the loading direction^[25].

The ordered filling method was used to build the cortex part. The distribution position (x_i, y_i) of cortex particles in the cross-section of ORSS was determined by Equation (3), with $(r_2, 0)$ as the coordinate reference, as shown in Figure 6a. In addition, the z-axis coordinates on each layer were gradually increased by 1.8 mm compared to the previous layer. A coordinate calculation visualization program was proposed using Visual Basic 6.0 to obtain the coordinates of the cortex particle, as shown in Figure 6b. The three-dimensional coordinates were then imported into the Meta-particle to generate the cortex part in the EDEM software.

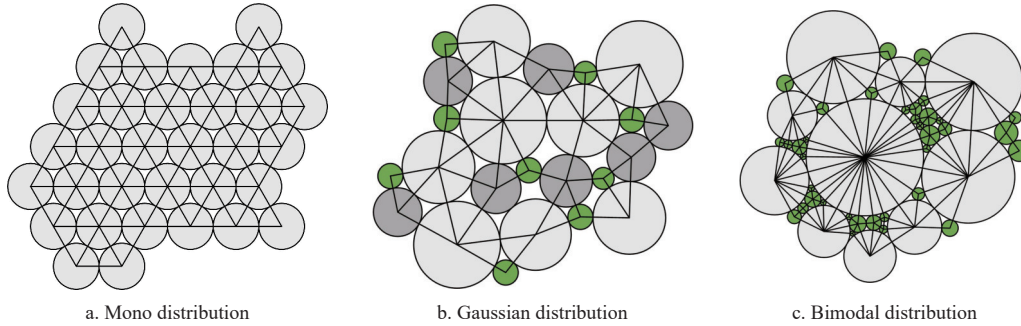


Figure 5 Schematic illustration of three types of packing structures

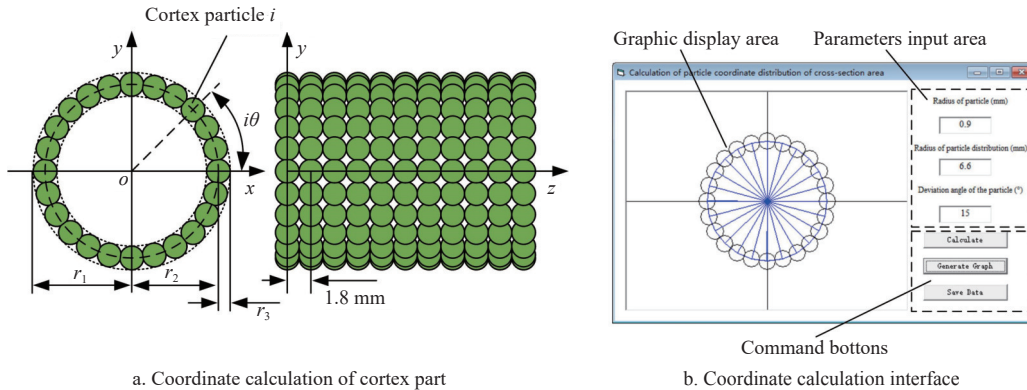


Figure 6 Schematic diagram of coordinate calculation of cortex part

$$\begin{cases} x_i = r_2 \sin i\theta \\ y_i = r_2 \cos i\theta, \quad i = 1, 2, \dots, 24 \\ r_2 = r_1 - r_3 \end{cases} \quad (3)$$

where, θ is the deviation angle of the cortex particle, ($^\circ$); r_1 is the radius of the stalk, mm; r_2 is the radius of the cortex particle position, mm; r_3 is the radius of the cortex particle, mm.

Additionally, a pith particle factory was built based on the ring-shaped cortex Meta-particle model, and a hollow cylinder was generated along the axis of the ring. The cylinder was then filled with particles to simulate the pith part, using two overlapping normal distributions, resulting in a final distribution that was not distinctly bimodal^[22]. To achieve sufficient breakage quality while maintaining computational economy, the particle-size ratio was chosen to be less than 2.5^[26]. Consequently, the mean sphere radii of large and smaller particles were set to 0.6 mm and 0.4 mm, respectively, with a standard deviation of 0.05 mm. The particle distribution is shown in Figure 7.

As shown in Figure 8a, a discrete element model of an oilseed rape shoot stalk with a length of 19.8 mm and a diameter of 15 mm was constructed. A total of 34 054 particles were generated with 156 638 bonds, including 264 cortex particles, 30 272 smaller

particles, and 3518 larger particles for the pith part. The average coordination number of the particle was 4.60, and the filling rate of the model was 43.30%. A higher coordination number can better capture the motion and the response characteristics of particles to external excitation^[15], thus more accurately reflecting the mechanical properties of oilseed rape shoot stalk. Moreover, the loading upper

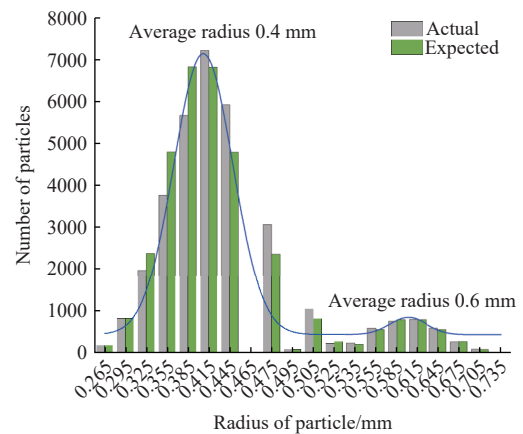


Figure 7 Particle distribution of ORSS discrete element model

and stationary bottom platens were modeled during the diametral compression test, respectively, as depicted in Figure 8b. According to Long et al.^[23], the loading speed had little effect on the

compression test within 0-500 mm/min. Therefore, the loading upper platen moved vertically downward at a speed of 500 mm/min to enhance the computational efficiency.

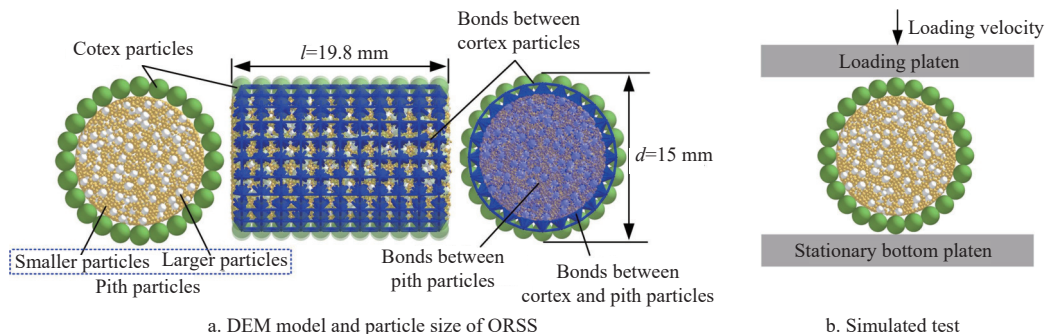


Figure 8 Diametral compression test model of ORSS

2.5 Micro-parameters of ORSS discrete element model

2.5.1 Intrinsic parameters

The intrinsic parameters of materials, such as Poisson’s ratio, density, and shear modulus, were relatively constant and were generally unaffected by other factors. These parameters were primarily obtained through relevant standard tests.

1) Poisson’s ratio μ

Based on previous studies^[21,5], Poisson’s ratio had little influence on the simulation results, so it was set to 0.4.

2) Density

The density ρ of the ORSS was evaluated to be 1028 kg/m³ using the Archimedes immersion method^[27].

3) Shear modulus G

The three-point bending test was performed to calculate the modulus of elasticity E , as shown in Figure 9a. The point linkage bending apparatus consisted of two supports 75 mm apart and a loading anvil fixed to the load cell of the texture analyzer. The contact part of the anvil had a 1.5 mm radius of curvature to reduce

the stress concentrations. The load cell measured the bending force applied at the center of the oilseed rape shoot stalk at a loading rate of 10 mm/min and a data acquisition frequency of 50 Hz.

The three-point bending test resulted in force-displacement curves, as shown in Figure 9b, with the linear elastic model fitted to the displacement range of 0-8 mm^[28]. Based on Edet^[29], the modulus of elasticity E was estimated using Equation (4) for a simple beam located at its center, and the second moment of area for the solid samples was calculated according to Equation (5).

$$E = \frac{F_b l^3}{48\delta I_b} \tag{4}$$

$$I_b = \frac{\pi}{64} (d_f^4) \tag{5}$$

where, F_b is the loading force, N; l is the distance between the support points, mm; δ is the deflection of the ORSS samples, mm; I_b is the second moment of the area, mm⁴; d_f is the diameter of the ORSS samples, mm.

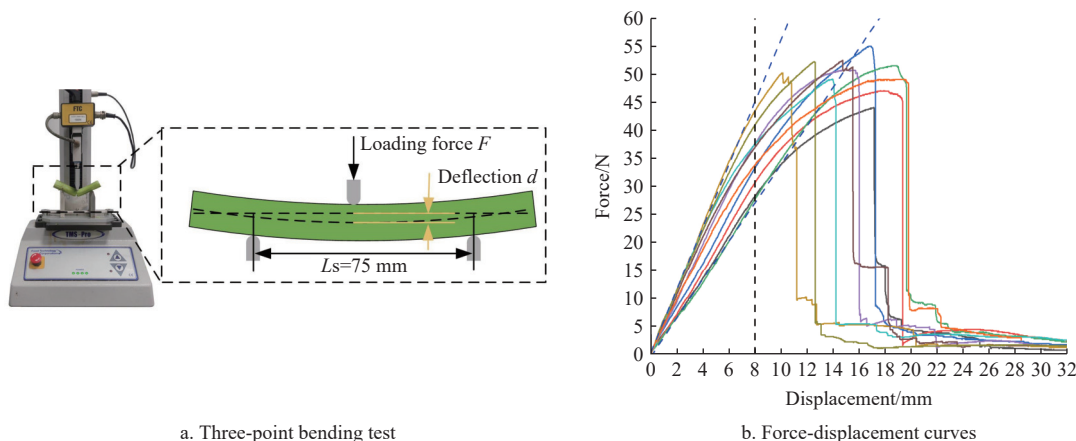


Figure 9 Three-point bending test

The shear modulus G was calculated from Equation (6) as follows^[9]:

$$G = \frac{E}{2(1+\mu)} \tag{6}$$

Additionally, the results of the three-point bending test and the intrinsic parameters of the ORSS are summarized in Table 1 and Table 2, respectively.

2.5.2 Value range of contact parameters and bonding parameters for calibration

Contact and bonding parameters are key micro-parameters for

bonded particle model simulation. Their accurate and reasonable definition affects the reliability of the final results. However, due to other factors, direct measurement of the discrete element parameters to be calibrated may not meet the test conditions^[14]. Therefore, the test design method was used to calibrate the contact parameters (coefficient of restitution, coefficient of static friction, and coefficient of rolling friction) and the five bonding parameters (normal stiffness per unit area, shear stiffness per unit area, critical normal stress, critical shear stress, and bonded disk radius). Table 3 lists the value range of relevant parameters for the simulation test, which was determined based on the previous literature^[12,21,30].

Table 1 Results of the three-point bending test^{bl}

No	The second moment of area/ mm ⁴	Loading force/N	Modulus of elasticity/ ($\times 10^6$ Pa)
1	2714.59	28.38	11.49
2	2654.91	30.80	12.75
3	3957.03	33.29	9.24
4	4361.50	27.79	7.00
5	2672.36	37.69	15.49
6	2429.20	43.48	19.67
7	3896.33	37.62	10.61
8	3285.90	37.09	12.40
9	2971.04	41.07	15.19
10	2700.46	33.83	13.76
Average value			12.76

Note: Deflection is 8 mm for the three-point bending test; the test was repeated 10 times.

Table 2 Intrinsic parameters

Parameters	Values	
	Steel	Oilseed rape shoot stalks
μ	0.3	0.4
G/Pa	7.94×10^{10}	4.56×10^6
$\rho/\text{kg}\cdot\text{m}^{-3}$	7850	1028

Table 3 Values of contact parameters for discrete element model of ORSS

Category	Properties	Type	Levels of parameters		
			Low (-1)	Medium (0)	High (+1)
Contact parameters	Coefficient of restitution	ORSS-ORSS	0.1	0.3	0.5
		ORSS-steel	0.1	0.4	0.7
	Coefficient of static friction	ORSS-ORSS	0.2	0.5	0.8
		ORSS-steel	0.2	0.5	0.8
	Coefficient of rolling friction	ORSS-ORSS	0.1	0.3	0.5
		ORSS-steel	0.1	0.3	0.5
Bonding parameters	Normal stiffness per unit area/ $\text{N}\cdot\text{m}^{-3}$		3.2×10^7	4.8×10^7	6.4×10^7
	Shear stiffness per unit area/ $\text{N}\cdot\text{m}^{-3}$		3.2×10^7	4.8×10^7	6.4×10^7
	Critical normal stress/Pa		3.0×10^8	6.5×10^8	1.0×10^9
	Critical shear stress/Pa		3.0×10^8	6.5×10^8	1.0×10^9
	Bonded disk radius/mm		0.6	0.8	1.0

2.6 Calibration procedure for relevant parameters of simulation test

The multi-parameters joint calibration is a reverse calibration method that simultaneously calibrates multiple parameters^[31]. The calibration procedure is complex and involves the test design method, establishing the relationship between the test indices and the parameters^[32,33]. The calibration procedure can be summarized into three steps: First, the diametral compression test provided the force-deformation curve and the rupture force, used as simulation test indices for parameter calibration. Second, the steepest ascent experiment narrowed the range of significant parameters obtained by the Plackett-Burman design. Third, the central composite design built the objective function that reflected the relationship between the simulation and the test results under different combinations of parameters. The optimal parameter combination was determined by satisfying the objective function and verified by comparison with the physical test results.

2.6.1 Plackett-Burman design

To identify the most important parameters of the simulation test, a Plackett-Burman design (a type of screening design) was

used to screen important parameters that significantly affected the simulation test index of rupture force. The factor levels and scheme of the design are listed in Table 3 and Table 4, respectively. The maximum value of each factor was coded as high level (+1), the minimum value was coded as low level (-1), and the center points as 0 levels. A total of 25 experimental simulation test runs were designed using Minitab Statistical Software (Minitab, LLC, USA).

Table 4 Experimental design and results of the Plackett-Burman design test

Run	Factors											Response
	A	B	C	D	E	F	G	H	J	K	L	Rupture force/N
1	-1	+1	+1	+1	+1	+1	-1	-1	-1	-1	+1	75.23
2	+1	+1	-1	+1	-1	+1	+1	+1	+1	+1	-1	43.53
3	+1	-1	-1	-1	-1	+1	-1	+1	-1	-1	+1	86.28
4	-1	+1	-1	-1	+1	+1	-1	-1	+1	+1	-1	20.22
5	+1	+1	+1	+1	+1	-1	-1	-1	-1	+1	-1	20.70
6	+1	+1	-1	-1	+1	+1	-1	+1	-1	+1	+1	119.17
7	-1	+1	-1	+1	+1	+1	+1	+1	-1	-1	-1	44.29
8	0	0	0	0	0	0	0	0	0	0	0	62.60
9	+1	-1	+1	-1	+1	+1	+1	+1	+1	-1	-1	34.99
10	-1	-1	-1	+1	-1	+1	-1	-1	+1	+1	-1	15.24
11	-1	-1	+1	+1	-1	-1	+1	+1	-1	+1	-1	31.59
12	-1	-1	+1	+1	-1	+1	-1	+1	+1	+1	+1	89.63
13	+1	-1	+1	-1	-1	+1	+1	-1	-1	+1	+1	90.53
14	+1	-1	-1	+1	+1	-1	+1	-1	+1	+1	+1	63.45
15	-1	+1	+1	-1	-1	+1	+1	-1	+1	-1	+1	115.41
16	+1	+1	+1	+1	-1	-1	-1	-1	+1	-1	+1	75.28
17	+1	+1	+1	-1	-1	-1	-1	+1	-1	+1	-1	32.06
18	+1	-1	-1	+1	+1	-1	-1	+1	+1	-1	+1	69.44
19	+1	-1	+1	+1	+1	+1	+1	-1	-1	-1	-1	24.09
20	-1	-1	+1	-1	+1	-1	-1	+1	+1	-1	-1	24.48
21	-1	-1	-1	-1	-1	-1	-1	-1	-1	-1	-1	21.78
22	+1	+1	-1	-1	-1	-1	+1	-1	+1	-1	-1	31.71
23	-1	+1	+1	-1	+1	-1	+1	+1	+1	+1	+1	188.00
24	-1	+1	-1	+1	-1	-1	+1	+1	-1	-1	+1	184.42
25	-1	-1	-1	-1	+1	-1	+1	-1	-1	+1	+1	71.05

2.6.2 Steepest ascent design

The steepest ascent design was used to search for a new region of essential parameters based on the Plackett-Burman design test results, improving the accuracy and validity of the simulation results. The relative error R_E of the rupture force between the physical and simulation tests was used as an evaluation index to narrow down the range of the parameters, calculated by Equation (7).

$$R_E = \frac{|F_{SC} - F_C|}{F_C} \times 100\% \quad (7)$$

where, F_C is the average rupture force of the physical test, N; F_{SC} is the rupture force of the simulated test, N.

2.6.3 Central composite design

The central composite design was conducted to capture the nonlinear relationship between the input factors of simulation test parameters, which were screened and improved by the Plackett-Burman design and steepest ascent design, and the output response of rupture force in the compression simulation test. It estimated the main effects and interactions and determined the optimal simulation parameters.

A second-order polynomial equation indicates the predicted response (rupture force) as a function of independent variables by Equation (8).

$$y = \beta_0 + \beta_1 x_1 + \beta_2 x_2 + \beta_3 x_3 + \beta_{11} x_1^2 + \beta_{22} x_2^2 + \beta_{33} x_3^2 + \beta_{12} x_1 x_2 + \beta_{13} x_1 x_3 + \beta_{23} x_2 x_3 \quad (8)$$

where, y is response values; β_i , β_{ij} , and β_{jk} are the values of linear, quadratic, and interactive coefficients, respectively, the values of i , j , and $k \in [0,3]$; β_0 is a constant.

3 Results and analysis

3.1 Loading force-displacement curve

The diametral compression test and the loading force-displacement curve are shown in Figures 10a and 10b, respectively. The loading force-displacement relationship was described in four stages: elastic stage, linear elastic stage, fracture failure stage, and compression strengthening stage. Initially, the compression force

gradually increased with the displacement, indicating that the ORSS structure started to bear the load. The deformation was insensitive to the force, possibly due to the ORSS undergoing dehydration and deformation under external pressure^[10]. When the force reached point A, the slope of the curve raised and remained constant in the linear elastic stage, where the ORSS structure remained uniformly stressed and slipped under the continuous loading force. As displacement increased, the force reached the first breakage point B, representing a transition between the linear elastic deformation and fracture failure stage. The compressive force dropped sharply and then gradually increased. This may be attributed to the compressive force exceeding the bond strength of the ORSS structure, resulting in fracture failure. However, the broken stalk was tightly compressed under the continuous load, leading to a secondary increase in the curve. The model had regained its resistance to deformation, entering and remaining in the compression strengthening stage until the end of the experiment.

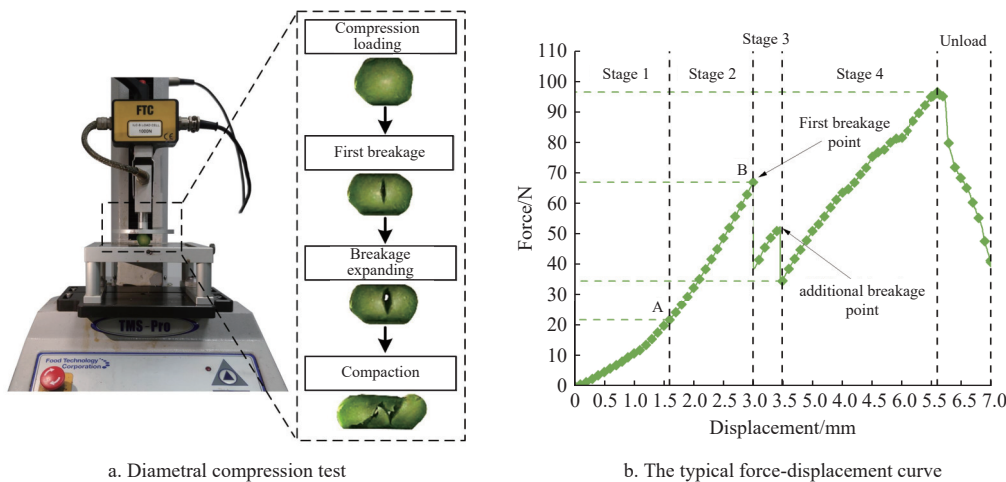


Figure 10 The diametral compression test

The changing trend in the force-displacement relationship curves closely aligned with the results reported for other crop stalks^[34,12]. The rupture force ranged from 45.56 to 74.25 N, with an average value of 62.92 N and a standard deviation of 8.70 N. Additionally, the average deformation at the rupture force point was 3.63 mm, with a standard deviation of 0.73 mm.

3.2 Selecting significant parameters

The data were analyzed using Minitab software. Table 4 lists the randomized design table and results of the Plackett-Burman design, while the analysis of variance (ANOVA) of the results is presented in Table 5. Moreover, the Pareto chart is displayed in Figure 11a, which shows the absolute values of the standardized effects, ranked from the most significant to the least. The factors bonded disk radius L , coefficient of static friction between particles of ORSS B , shear stiffness per unit area H , and normal stiffness per unit area G crossed the blue reference line, indicating statistical significance at a 95% confidence level. Additionally, the main effects plot (Figure 11b) demonstrates that the significant factors B , G , H , and L increased rupture force, with normal stiffness L having the largest effect, followed by B . In Table 4, the rupture force varied under different parameter combinations, ranging from 15.24 N to 188.00 N, which corresponded to the range of physical test results (45.56-74.25 N). Additionally, the simulation test results for Nos. 8, 14, and 18 in Table 5 were close to the average value (62.92 N) from the physical compression test.

Table 5 ANOVA of Plackett-Burman design test

Source	Degree of freedom	Adjusted sum	Adjusted mean square	F-value	p-value
Model	12	46 729.5	3894.1	6.83	0.001**
Linear	11	46 721.3	4247.4	7.45	0.001**
A	1	1505.9	1505.9	2.64	0.130
B	1	4468.2	4468.2	7.83	0.016*
C	1	41.1	41.1	0.07	0.793
D	1	406.6	406.6	0.71	0.415
E	1	162.0	162.0	0.28	0.604
F	1	127.7	127.7	0.22	0.645
G	1	3117.9	3117.9	5.47	0.038*
H	1	4352.2	4352.2	7.63	0.017*
J	1	37.0	37.0	0.06	0.803
K	1	0.2	0.2	0.00	0.985
L	1	32 502.5	32 502.5	56.98	<0.0001**
Curvature	1	8.2	8.2	0.01	0.907
Error	12	6845.4	570.4		
Total	24	53 574.8			

Note: A: Coefficient of restitution between particles of ORSS; B: Coefficient of static friction between particles of ORSS; C: Coefficient of rolling friction between particles of ORSS; D: Coefficient of restitution between particles of ORSS and steel; E: Coefficient of static friction between particles of ORSS and steel; F: Coefficient of rolling friction between particles of ORSS and steel; G: Normal stiffness per unit area, N/m²; H: Shear stiffness per unit area, N/m²; J: Critical normal stress, Pa; K: Critical shear stress, Pa; L: Bonded disk radius, mm. **highly significant ($p < 0.01$); *significant ($p < 0.05$).

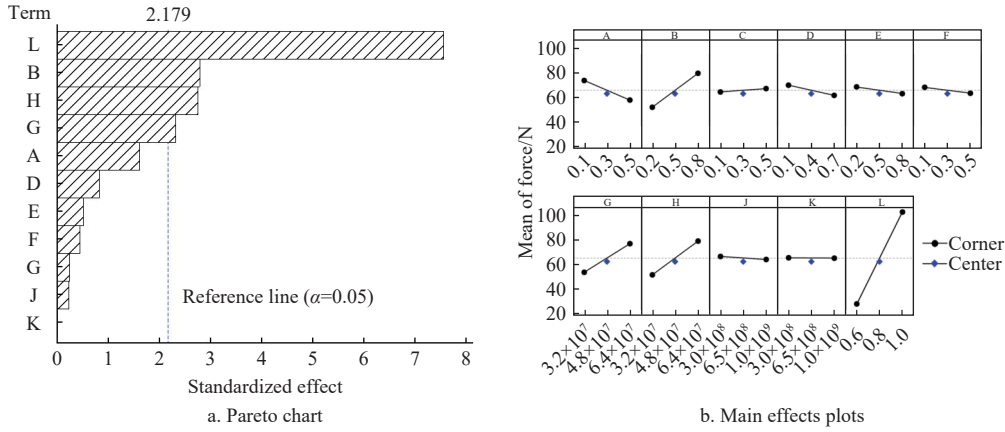


Figure 11 T-value of effect for parameters

3.3 Determination of the optimal ranges of significant parameters

The steepest ascent test was conducted based on the four significant parameters identified in the Plackett-Burman test, including the bonded disk radius L , the coefficient of static friction between ORSS B , the shear stiffness per unit area H , and normal stiffness per unit area G . The range of parameters and step size were assessed similarly to the method described by Gramacy^[35]. Seven groups of diametral compression simulation tests were uniformly conducted to identify the potential optimal parameters region, with other parameters held at intermediate values. Table 6 shows the path and results of the steepest ascent test. As parameters accumulated, the relative error decreased, reaching a minimum of 5.72% in the fourth group before increasing. Therefore, the parameter values from the third and fifth groups were used as initial ranges for the central composite design to estimate optimal parameter values.

Table 6 Path and results of the steepest ascent test

No.	Factors				Rupture force/N		Relative error
	B	G	H	L	Simulation test	Physical test	
Base	0.20	3.20×10^7	3.20×10^7	0.60			
1	0.28	3.65×10^7	3.64×10^7	0.65	24.65		60.82%
2	0.36	4.10×10^7	4.08×10^7	0.70	33.63		46.55%
3	0.45	4.55×10^7	4.52×10^7	0.75	48.10		23.55%
4	0.53	5.00×10^7	4.96×10^7	0.80	66.52	Average value	5.72%
5	0.61	5.45×10^7	5.40×10^7	0.85	87.51	62.92	39.08%
6	0.69	5.91×10^7	5.83×10^7	0.90	115.33		83.30%
7	0.78	6.36×10^7	6.27×10^7	0.95	123.03		95.53%

The displacement-force curves of the steepest ascent test are shown in Figure 12. The curves for Nos. 3, 4, 5, and 6 exhibited a decreasing and then increasing trend after the breakage point, unlike the other curves. Moreover, the rupture force and the corresponding displacement increased with higher simulation parameter values. This trend was due to the increasing values of compressive stiffness along the bond's principal axis and shear stiffness in the orthogonal plane to the bond's principal axis, which generated higher bond forces and stresses^[18,11]. The results indicate that the parameters not only affected the rupture force but also significantly influenced the displacement-force curve trend.

3.4 Determination of optimal value of the simulation test parameters

Response surface methodology is a statistical and mathematical technique used to build models and optimize the levels of independent variables^[36]. The Design Expert software (version 12.0.3.0) was

employed to analyze the results of the central composite design and calculate the values of coefficients of determination.

3.4.1 Fitting the model

The central composite design consisted of 27 tests, including center tests to estimate the test error and 24 tests to analyze the effects of the independent variables: bonded disk radius L , the coefficient of static friction between particles of ORSS B , the shear stiffness per unit area H , and normal stiffness per unit area G . Table 7 lists the experimental design and the response values.

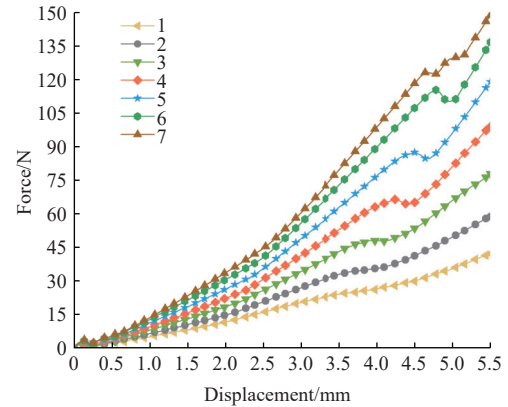


Figure 12 Effects of parameters on rupture force of the steepest ascent test

The ANOVA results for the rupture force are listed in Table 8. The significant independent variables affecting the rupture force, in descending order of importance, were the bonded disk radius L , normal stiffness per unit area G , the shear stiffness per unit area H , and the coefficient of static friction between particles of ORSS B . Furthermore, an F -test was carried out at a 95% confidence interval. The regression equation for the rupture force response value, derived from the experimental data after removing insignificant terms, was as Equation (9).

$$y = 66.52 + 5.44A + 1.06B + 2.01C + 1.21D - 0.66AB + 0.39AC + 0.74AD + 0.86BD - 0.25A^2 \quad (9)$$

Statistical analysis results (Table 8) reveal that the model F -value of 282.2718 indicated significant model performance, with a negligible probability (0.01%) of such a large value occurring due to noise. Moreover, the coefficient of determination (R^2), adjusted coefficient of determination (R^2_{Adj}), and predicted coefficient of determination (R^2_{Pre}) were all greater than 0.98, close to 1, suggesting a good fit of the experimental data with a quadratic polynomial model (Equation (9)).

Table 7 Experimental design and response values of central composite design test

Std.	Run	Factors				Response
		<i>L</i>	<i>B</i>	<i>H</i>	<i>G</i>	Rupture force/N
14	1	1	-1	1	1	74.57
17	2	-2	0	0	0	54.76
16	3	1	1	1	1	77.22
9	4	-1	-1	-1	1	57.31
8	5	1	1	1	-1	72.01
4	6	1	1	-1	-1	65.81
18	7	2	0	0	0	76.10
15	8	-1	1	1	1	65.45
13	9	-1	-1	1	1	60.32
2	10	1	-1	-1	-1	67.93
11	11	-1	1	-1	1	61.88
27	12	0	0	0	0	66.52
26	13	0	0	0	0	66.52
19	14	0	-2	0	0	63.63
7	15	-1	1	1	-1	62.77
25	16	0	0	0	0	66.52
3	17	-1	1	-1	-1	59.37
10	18	1	-1	-1	1	69.87
1	19	-1	-1	-1	-1	57.35
23	20	0	0	0	-2	65.29
21	21	0	0	-2	0	61.77
24	22	0	0	0	2	69.00
12	23	1	1	-1	1	73.12
20	24	0	2	0	0	67.65
5	25	-1	-1	1	-1	60.52
22	26	0	0	2	0	69.63
6	27	1	-1	1	-1	72.30

Table 8 ANOVA of central composite design test^[a]

Source	Sum of squares	Degree of freedom	Mean of square	<i>F</i> -value	<i>p</i> -value ^[b]
Model	903.8245	14	64.55 889	282.2718	<0.0001**
<i>L</i>	710.0288	1	710.0288	3104.469	<0.0001**
<i>B</i>	27.09 375	1	27.09 375	118.4624	<0.0001**
<i>H</i>	96.9624	1	96.9624	423.9501	<0.0001**
<i>G</i>	35.28 375	1	35.28 375	154.2717	0.0001**
<i>LB</i>	6.8644	1	6.8644	30.01 332	0.0001**
<i>LH</i>	2.418 025	1	2.418 025	10.57 237	0.007**
<i>LG</i>	8.673 025	1	8.673 025	37.9212	<0.0001**
<i>BH</i>	0.255 025	1	0.255 025	1.115 05	0.312
<i>BG</i>	11.79 923	1	11.79 923	51.58 993	<0.0001**
<i>HG</i>	0.1936	1	0.1936	0.84 648	0.376
<i>L</i> ²	1.335 556	1	1.335 556	5.839 473	0.033*
<i>B</i> ²	0.833 89	1	0.83 389	3.646 029	0.080
<i>H</i> ²	0.712 156	1	0.712 156	3.113 772	0.103
<i>G</i> ²	0.680 045	1	0.680 045	2.973 372	0.110
Residual	2.744 542	12	0.228 712		
Lack of fit	2.744 542	10	0.274 454		
Pure error	0	2	0		
Cor total	906.569	26			

Note: ^[a] $R^2_{Adj} = 0.9934$; $R^2_{Pre} = 0.9826$;

^[b] $p < 0.01$ (highly significant, represented by **); $p < 0.05$ (significant, represented by *).

Furthermore, the residual diagnostics of the quadratic polynomial model are presented in Figure 13a, which shows a rough pattern of the data points, indicating normality in the error term and the validity of the established model between the independent variables and response value. Additionally, Figure 13b shows the linear correlation of the actual and predicted data, reflecting the statistical accuracy and predictive power of the model for the rupture force.

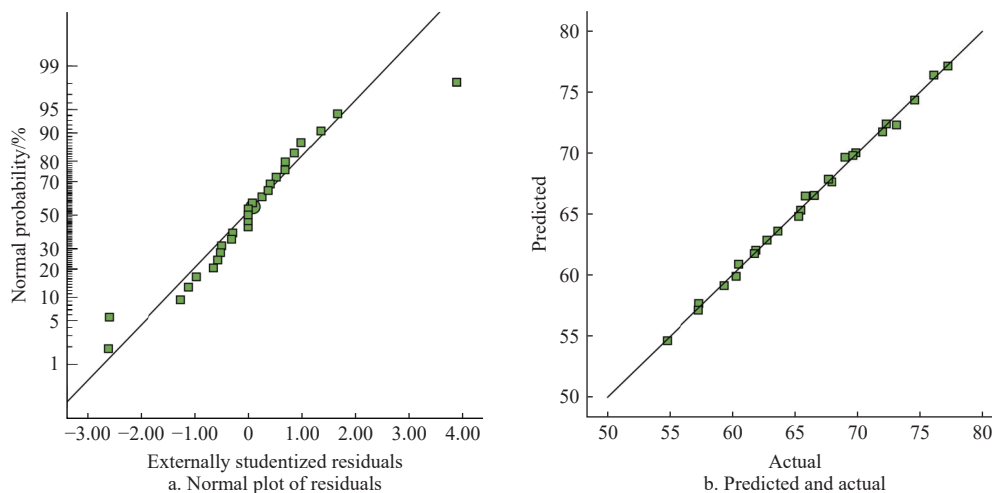


Figure 13 Residual diagnostics of the quadratic model

3.4.2 Interaction effect analysis

As listed in Table 8, in this study, the rupture force in the simulation test depended on the bonded disk radius, which significantly affected rupture force at the linear ($p < 0.01$), quadratic ($p < 0.05$), and interaction levels with the coefficient of static friction between particles of ORSS ($p < 0.01$), shear stiffness per unit area ($p < 0.01$), and normal stiffness per unit area ($p < 0.01$), respectively. This result is consistent with reported modeling parameters for cotton stalks^[10]. Additionally, other significant independent variables include the linear terms of the coefficient of static friction

between particles of ORSS, the normal stiffness per unit area, and the shear stiffness per unit area ($p < 0.01$), as well as the interaction term between the coefficient of static friction between particles of ORSS and normal stiffness per unit area ($p < 0.01$).

To illustrate the interactive effects between the four independent variables, response surface graphs were generated by varying two independent variables within experimental ranges, while keeping the other variables at the center point, as shown in Figure 14. Figures 14a and 14b show that the rupture force increased with the increase in the bonded disk radius, coefficient of

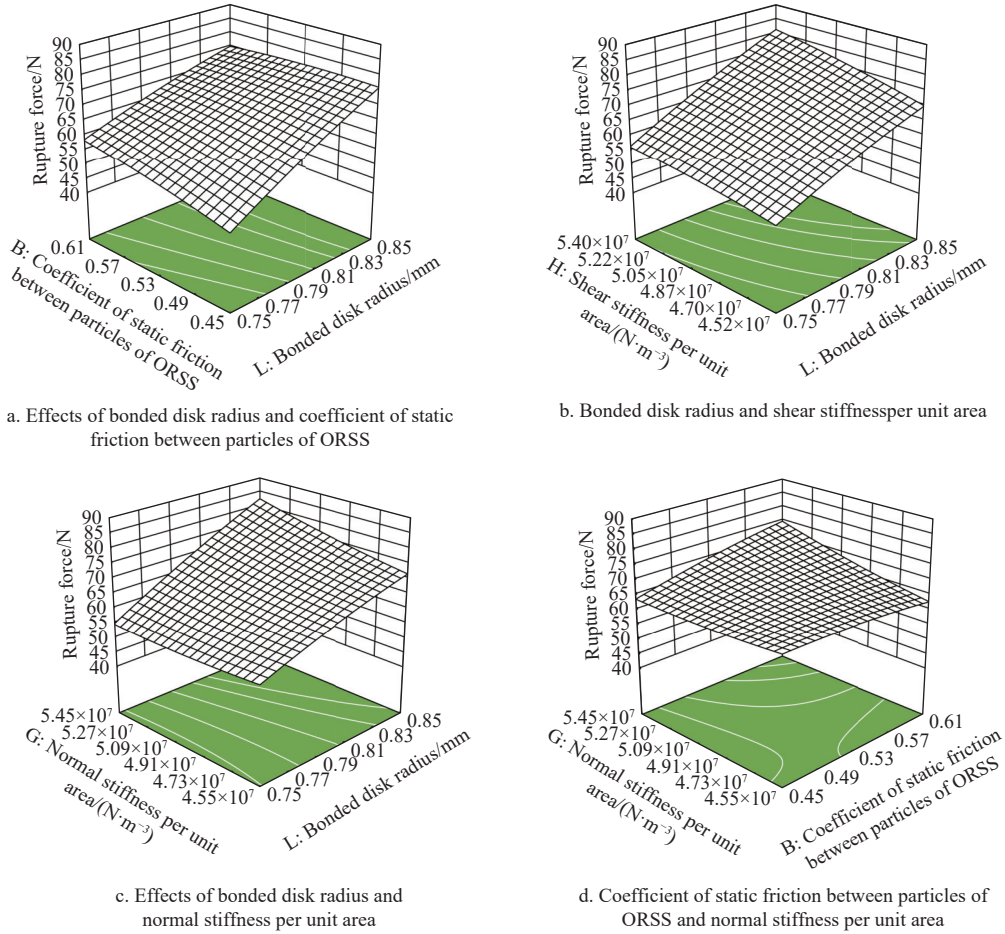


Figure 14 Response surface of rupture force

static friction between particles of ORSS, and shear stiffness per unit area, respectively. Moreover, the bonded disk radius had a more significant impact on the rupture force than the coefficient of static friction between particles of stalk and normal stiffness per unit area. This increase was due to higher stiffness values producing higher bond forces and stresses, and to the increase in bonded disk radius, resulting in a larger contact area, consistent with the theoretical equation of the bonded particle model (Equation (1)). Figures 14c and 14d depict that the positive effect of bonded disk radius on the rupture force became more pronounced with increasing normal stiffness per unit area, while the coefficient of static friction between the particles of ORSS had a relatively small influence on the interaction effects of rupture force.

3.4.3 Determination of the optimal parameter combination

According to the results of the Plackett-Burman test and the steepest ascent test, the optimal parameter ranges for the bonded disk radius, coefficient of static friction between particles of ORSS, shear stiffness per unit area, and normal stiffness per unit area were determined to be 0.75-0.85 mm, 0.45-0.61, 4.52×10^7 - 5.40×10^7 Pa, and 4.55×10^7 - 5.45×10^7 Pa, respectively. The Design Expert software performed numerical optimization using the average value of rupture force (62.92 N) from the physical diametral compression test as the optimization target. The objective and constraint functions are provided in Equation (10).

$$\left\{ \begin{array}{l} \text{s.t.} \left\{ \begin{array}{l} 0.75 \leq L \leq 0.85 \\ 0.45 \leq B \leq 0.61 \\ 4.52 \times 10^7 \leq H \leq 5.40 \times 10^7 \\ 4.55 \times 10^7 \leq G \leq 5.45 \times 10^7 \end{array} \right. \quad (10) \\ \text{Target value of } y = 62.92 \end{array} \right.$$

A total of 100 solutions were identified at various levels, and the solution with the highest desirability value, close to 1, indicated that each variable met the criteria effectively. This solution was selected as the optimized result. Consequently, the combined optimized preparation conditions were: normal stiffness per unit area of 4.61×10^7 Pa, shear stiffness per unit area of 5.21×10^7 Pa, bonded disk radius of 0.78 mm, and a coefficient of static friction between ORSS particles of 0.47.

3.5 Validation of calibration parameters

To verify the validity and accuracy of the optimized parameter combination, a diametral compression simulation test was conducted under the optimized conditions. The standard deviation between the rupture force obtained from the physical and simulation diametral compression tests was used as the evaluation index.

Figure 15 shows the diametral compression deformation process in both the physical (Figure 15a) and simulation test (Figure 15b). As the loading displacement increased, the compressive forces (normal), represented in red, gradually diffused along the x -axis centered on the y -axis, and the curvature of the force chains increased. Thus, the breakage initiated at the center of the oilseed rape shoot stalk agglomerate and propagated vertically towards the loading plates, breaking the bonds colored in blue due to instantaneous resultant compressive force (normal). Continuous deformation of the agglomerate caused many bonds at the breaking part to fail, resisting the compressive force. Therefore, the compressive force (normal) was localized into two symmetric, arch-shaped chains. As the agglomerate underwent further compaction, the normal compressive force distribution became more uniform. The deformation of the oilseed rape shoot stalk observed in the simulation test was consistent with the results of the physical test,

reflecting the transmission of the force chain during the diametral compression process.

The displacement-force curves of the simulation test based on the optimized parameters, as well as of the physical test, are shown in Figure 16a. The linear-elastic stage of both curves exhibited a consistent trend. The rupture force of the simulation test (58.80 N) was 6.5% lower than the average rupture force of the physical test (62.92 N). The relative error was less than 10%, indicating the accuracy of the calibration parameters and the reliability of the simulated diametral compression test^[4,13]. However, as seen in Figure 16a, the simulation curve had a larger loading displacement corresponding to the rupture force than the physical test curve. This discrepancy may be due to the difference in diameter and shape between the samples and the different deformation positions that

provided the ultimate support force^[18].

During the physical compression process, when the compressive force exceeded the bonding strength between the cells of the oilseed rape shoot stalks, a rapid rupture occurred, and the compressive force dropped precipitously. In the simulation test, the number of intact bonds represented the resistance to the loading force. Figure 16b shows the relationship between the loading displacement and the number of intact bonds. The number of intact bonds decreased gradually during the elastic and linear elastic stages. In the breakage stage, the number of intact bonds decreased sharply, with the slope of the curve intuitively reflecting this change. Thus, due to the difference in the biomechanical properties of the ORSS and the higher computational time required for the simulation test, this displacement deviation was deemed acceptable^[18,5].

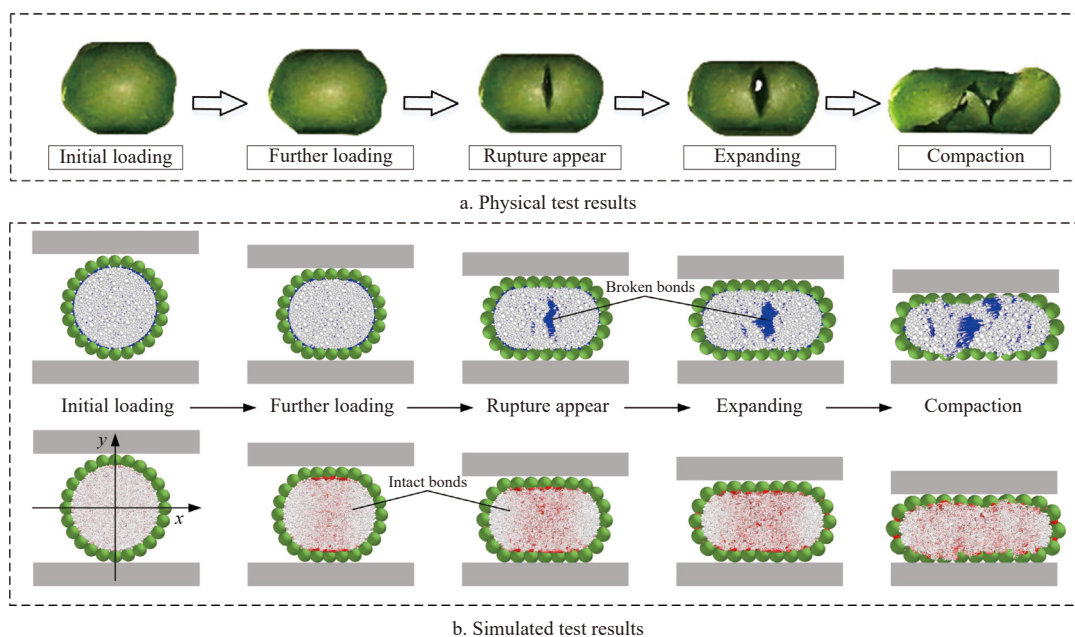


Figure 15 Typical characteristics of ORSS in diametral compression test

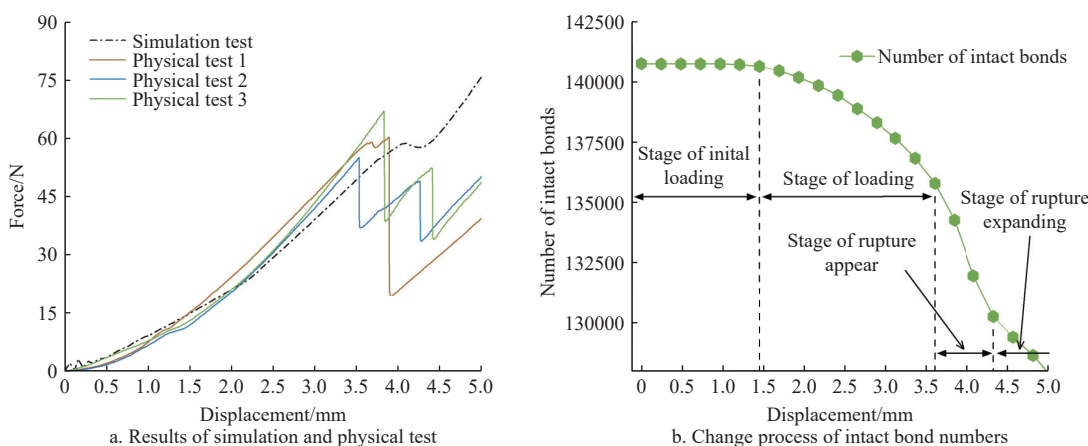


Figure 16 Comparison of simulation and physical test

4 Conclusions and discussion

In this study, the mechanical properties of oilseed rape shoot stalk during the harvesting period were tested and simulated to provide references for the design and development of harvesting machinery. The results led to the following conclusions:

1) A bond-particle model of oilseed rape shoot stalk with a diameter of 15 mm was constructed based on the Hertz-Mindlin

model. The particles in this model were filled with a combination of ordered and bimodal distributions. Physical and simulated diametral compression tests were conducted to study the mechanical behavior of oilseed rape shoot stalk, using the average rupture force F_C from the physical test as the response value for the simulation. Furthermore, the Plackett-Burman experimental design was applied to determine the main effects of 11 contact and bonding parameters. Additionally, the range and the effects of the most important factors

were investigated using the steepest ascent test.

2) The significant factors of bonded disk radius, normal stiffness per unit area, shear stiffness per unit area, and coefficient of static friction between stalk particles were analyzed and calibrated using central composite experimental design tests. A mathematical regression model with the response value of rupture force was established. The ANOVA results showed that the equation was reliable, and the primary and secondary factors influencing the rupture force were the bonded disk radius, shear stiffness per unit area, normal stiffness per unit area, and the coefficient of static friction between particles of oilseed rape shoot stalk.

3) The optimal parameter combination included a bonded disk radius of 0.78 mm, a normal stiffness per unit area of 4.61×10^7 Pa, a shear stiffness per unit area of 5.21×10^7 Pa, and a coefficient of static friction between particles of ORSS of 0.47. The simulated rupture force with these parameters was 58.80 N, showing an acceptable error of 6.5% compared with the physical result of 62.92 N. Additionally, the simulated and actual loading force-displacement curves exhibited a consistent trend, and the simulated results accurately reflected changes in the normal force chain during compression.

Agglomerates of discrete element models, constructed using different filling methods, can mostly meet the accuracy of simulation values within a reasonable parameter range through parameter calibration^[23]. However, there were still some limitations. Firstly, constructing an agglomerate model required additional consideration of agricultural material model parameters such as porosity, texture, particle size, particle number, and compaction pressure^[37,38]. Furthermore, obtaining detailed information on the physical and mechanical properties of different crop varieties, such as moisture contents, variations in plant structure, and structural parameters, was crucial for constructing agglomerates of discrete element models. Additionally, the parallel bond configuration in the simulation software used for the model provided limited options for accurately setting the active bond parameters for the materials, leading to a trade-off between simulation accuracy and time^[18].

In general, the proposed model of the oilseed rape shoot stalk provided insights into the propagation of compressive-force chains during the diametral compression test. This helped to comprehend the compression failure mechanism and predict the compressive properties of oilseed rape shoot stalks. The model in this study can be effectively used to simulate the interaction between the oilseed rape stalk and harvesting equipment. Additionally, the modeling method and process can be applied to other plant stalk materials. In future research, the model will be enhanced by incorporating the shear, tension, and bending mechanical properties of oilseed rape shoots from different varieties, with different moisture content, maturity, and position. Separate models will also be constructed for the cortex and pith parts, with calibrations performed under multiple loading methods, which will be the key research focus. With the ongoing and increasing research, methods for constructing agglomerates of discrete element models for agriculture materials are expected to become more efficient and accurate.

Acknowledgements

This work was funded by the National Natural Science Foundation of China (Grant No. 52205270 and No. 52075210), the Natural Science Foundation of Hubei Province (Grant No. 2023AFB852), the Fundamental Research Funds for the Central Universities (Grant No. 2662023GXQD002), and China Agriculture

Research System of MOF and MARA (Grant No. CARS-12).

[References]

- [1] Shi R, Pang C K, Wu X, Zhao X Z, Chen F, Zhang W, et al. Genetic dissection and germplasm selection of the low crude fiber component in *Brassica napus* L. shoots. *Foods*, 2023; 12(2): 403.
- [2] Wang H Z. New-demand oriented oilseed rape industry developing strategy. *Chinese Journal of Oil Crop Sciences*, 2018; 5(40): 613–617. (in Chinese)
- [3] Huang H L, Shi Y M, Liu T, Zhou Y. Oilseed-vegetable-dual-purpose rape key technology research and its application prospect analysis. *Agricultural Sciences*, 2014; 5(13): 1291–1295.
- [4] Su Y, Xu Y, Cui T, Gao X J, Xia G Y, Li Y B, et al. Determination and interpretation of bonded-particle model parameters for simulation of maize kernels. *Biosystems Engineering*, 2021; 210: 193–205.
- [5] Xie W, Ouyang C, Jiang P, Meng D X, Luo H F. Calibrating and optimizing the discrete element parameters for clamping section stems during rape shoot harvesting. *Transactions of the CSAM*, 2024; 40(7): 104–116. (in Chinese)
- [6] Zhang X R, Hu X H, Liu J X, Yang Y M, Li Y. Calibration and verification of bonding parameters of banana straw simulation model based on discrete element method. *Transactions of the CSAM*, 2023; 54(5): 121–130. (in Chinese)
- [7] Jia H L, Deng J Y, Deng Y L, Chen T Y, Wang G, Sun Z J, et al. Contact parameter analysis and calibration in discrete element simulation of rice straw. *Int J Agric & Biol Eng*, 2021; 14(4): 72–81.
- [8] Peng C W, Chen J W, He X, Sun S L, Yin Y L, Chen Z. Discrete element modeling and verification of the simulation parameters for chopped hybrid *Broussonetia papyrifera* stems. *Int J Agric & Biol Eng*, 2024; 17(1): 23–32.
- [9] Xie K T, Zhang Z G, Wang F A, Yu X L, Wang C L, Jiang S F. Calibration and experimental verification of discrete element parameters of Panax notoginseng root. *Int J Agric & Biol Eng*, 2024; 17(4): 13–23. doi: 10.25165/j.ijabe.202417048122.
- [10] Zhao W S, Chen M J, Xie J H, Cao S L, Wu A B, Wang Z W. Discrete element modeling and physical experiment research on the biomechanical properties of cotton stalk. *Computers and Electronics in Agriculture*, 2023; 204: 107502.
- [11] Wang Y, Zhang Y T, Yang Y, Zhao H M, Yang C H, He Y, et al. Discrete element modelling of citrus fruit stalks and its verification. *Biosystems Engineering*, 2020; 200: 400–414.
- [12] Guo J, Karkee M, Yang Z, Fu H, Li J, Jiang Y L, et al. Discrete element modeling and physical experiment research on the biomechanical properties of banana bunch stalk for postharvest machine development. *Computers and Electronics in Agriculture*, 2021; 188: 106308.
- [13] Li X Y, Du Y F, Liu L, Zhang Y N, Guo D F. Parameter calibration of corncob based on DEM. *Advance Power Technology*, 2022; 33(8): 103699.
- [14] Wang X W, Li B, Xia R, Ma H Z. Engineering applications of discrete element method - operation analysis and optimization design of coal and agricultural machinery. Singapore: Springer Nature Singapore Pte Ltd., 2021; pp.6–7.
- [15] Hao J J, Long S F, Li H, Jia Y L, Ma Z K, Zhao J G. Development of discrete element model and calibration of simulation parameters for mechanically-harvested yam. *Transactions of the CSAE*, 2019; 35(20): 34–42. (in Chinese)
- [16] Grima A P, Wypych P W. Investigation into calibration of discrete element model parameters for scale-up and validation of particle-structure interactions under impact conditions. *Powder Technology*, 2011; 212(1): 198–209.
- [17] Zhang W X, Wang F Y. Parameter calibration of American ginseng seeds for discrete element simulation. *Int J Agric & Biol Eng*, 2022; 15(6): 16–22.
- [18] Shi Y Y, Jiang Y, Wang X C, Thuy N T D, Yu H M. A mechanical model of single wheat straw with failure characteristics based on discrete element method. *Biosystems Engineering*, 2023; 230: 1–15.
- [19] Wang S A, Yu Z H, Aorigele, Zhang W J. Study on the modeling method of sunflower seed particles based on the discrete element method. *Computers and Electronics in Agriculture*, 2022; 198: 107012.
- [20] ASABE S358.2, Measurement-Forages. St Joseph MI: American Society of Agricultural Engineers, 2006.
- [21] Liao Y T, Liao Q X, Zhou Y, Wang Z T, Jiang Y J, Liang F. Parameters

- calibration of discrete element model of fodder rape crop harvest in bolting stage. *Transactions of the CSAM*, 2020; 51(6): 73–82. (in Chinese)
- [22] Quist J, Evertsson C M. Cone crusher modelling and simulation using DEM. *Minerals Engineering*, 2016; 85: 92–105.
- [23] Long S F, Xu S M, Zhang Y J, Zhang J, Wang J. Effect of modeling parameters on the mechanical response of macroscopic crushing of agglomerate. *Powder Technology*, 2022; 408: 117720.
- [24] Liu Y G, Zhao J G, Yin B Z, Ma Z K, Hao J J, Yang X, et al. Discrete element modelling of the yam root-soil complex and its verification. *Biosystems Engineering*, 2022; 220: 55–72.
- [25] Kovács Á. Modelling of maize plant by the discrete element method. Doctor dissertation. Budapest: Budapest University of Technology and Economics, 2019; pp.6–7.
- [26] Wiącek J, Stasiak M, Parafiniuk P. Effective elastic properties and pressure distribution in bidisperse granular packings: DEM simulations and experiment. *Archives of Civil and Mechanical Engineering*, 2017; 17(2): 271–280.
- [27] de Araújo Carvalho E, Magalhães R R, Santos F L. Geometric modeling of a coffee plant for displacements prediction. *Computers and Electronics in Agriculture*, 2016; 123: 57–63.
- [28] Leblicq T, Vanmaercke S, Ramon H, Saeys W. Mechanical analysis of the bending behaviour of plant stems. *Biosystems Engineering*, 2015; 129: 87–99.
- [29] Edet U. Mechanical properties of hollow and solid wheat stems. Master dissertation. Saskatoon, Saskatchewan: University of Saskatchewan, 2015; pp.31–32.
- [30] Wan X Y, Liao Q X, Jiang Y J, Shan Y Y, Zhou Y, Liao Y T. Discrete element simulation and experiment of mechanized harvesting and chopping process for fodder rape crop harvest. *Journal of Jilin University (Engineering and Technology Edition)*, 2022; 52(11): 2735–2745. (in Chinese)
- [31] Aster R C, Borchers B, Thurber C H. Parameter estimation and inverse problems (Second Edition). Amsterdam: Elsevier, 2013; 376p.
- [32] Fang M, Yu Z H, Zhang W J, Cao J, Liu W H. Friction coefficient calibration of corn stalk particle mixtures using Plackett-Burman design and response surface methodology. *Powder Technology*, 2022; 396(PartB): 731–742.
- [33] Xia R, Li B, Wang X W, Li T J, Yang Z J. Measurement and calibration of the discrete element parameters of wet bulk coal. *Measurement*, 2019; 142: 84–95.
- [34] Khan M M R, Chen Y, Laguë C, Landry H, Peng Q, Zhong W. Compressive properties of Hemp (*Cannabis sativa* L.) stalks. *Biosystems Engineering*, 2010; 106(3): 315–323.
- [35] Gramacy R B. Gaussian process modeling, design and optimization for the applied sciences. Boca Raton, Florida: CRC Press, 2023; 560p.
- [36] Berger P D, Maurer R E, Celli G B. Experimental Design With Applications in Management, Engineering, and the Sciences (Second Edition). New York: Springer, 2017; 639p.
- [37] Horabik J, Wiącek J, Parafiniuk P, Stasiak M, Bańda M, Molenda M. Tensile strength of pressure-agglomerated potato starch determined via diametral compression test: Discrete element method simulations and experiments. *Biosystems Engineering*, 2019; 183: 95–109.
- [38] Horabik J, Wiącek J, Parafiniuk P, Stasiak M, Bańda M, Kobyłka R, et al. Discrete element method modelling of the diametral compression of starch agglomerates. *Materials*, 2020; 13(4): 932.